Electrochemical assessment of highly reversible SnO2 coated Zn metal anodes prepared via atomic layer deposition for aqueous Zn-ion batteries

Sang Hyuk Gong
  Korea Institute of Science and Technology (KIST)

Hyo Jin Lim
  Korea Institute of Science and Technology (KIST)

Ji Hyeon Lee
  Korea University

Yiseul Yoo
  Korea Institute of Science and Technology (KIST)

Seungho Yu
  Korea Institute of Science and Technology (KIST)

Hee-Dae Lim
  Korea Institute of Science and Technology (KIST)

Hyun Wook Jung
  Korea University

Jesse S. Ko
  Johns Hopkins University Applied Physics Laboratory

In Soo Kim
  Korea Institute of Science and Technology (KIST)

Hyung-Seok Kim
  hskim0227@kist.re.kr

  Korea Institute of Science and Technology (KIST)

Research Article

Additional Declarations: No competing interests reported.

Abstract

Aqueous electrochemical energy storage systems that rely on earth-abundant elements are considered as cost-effective alternatives to current lithium-ion batteries which have dominated the technological landscape. For zinc-based energy storage, dendrite growth is an underlying challenge that needs to be addressed to enact high performance and long-term stability. In the present study, we employ atomic layer deposition to produce a thin tin oxide layer that allows dendrite-free cycling for aqueous zinc-ion batteries. Tin oxide is particularly interesting as it provides two distinct advantages—dendrite-free cycling and mitigation of parasitic hydrogen gas evolution. The presence of the tin oxide layer leads to hydrogen gas suppression and homogeneous zinc plating/stripping, both of which are essential to improve the performance of zinc-ion batteries. When paired in a full-cell configuration with manganese oxide, this anode delivers a high specific capacity of 250 mAh g^{-1} at an imposed current rate of 30 mA g^{-1}. Through density functional theory calculations, we elucidate further that the adsorption energy of Zn for bare Zn is higher than that in the presence of a tin oxide layer.

Introduction And Background

Owing to the alarming growth of the energy storage sector, coupled with the developing electric vehicle market, the need for improved battery performance in terms of high energy, high power, and long-term stability is needed. Lithium-ion batteries are a strong contender for high performance energy storage; yet, this technology is plagued by potential explosion and stability issues derived from their flammable nature. Moreover, as lithium reserves are geographically limited, it is becoming increasingly difficult to meet current demands and therefore the costs are projected to rise exponentially. [1] As such, attention is being drawn to next-generation secondary batteries that are sourced from safe and abundant materials. To this end, researchers are seeking opportunities in alternative batteries with polyvalent (e.g., magnesium [2], calcium [3], zinc [4], and aluminum [5]) ions. Among these, we focus on aqueous secondary zinc-ion batteries (ZIBs) using environmentally-benign, earth-abundant transition metals.

Aqueous secondary ZIBs are particularly attractive for applications in vehicle electrification, grid storage, and wearable devices that operate in proximity to the human body, owing to their superior biocompatibility and safety characteristics. Zinc (Zn) is abundant in the Earth's crust, recyclable, cost effective, non-toxic, and has excellent chemical stability in aqueous electrolytes compared to alkali metals such as lithium or sodium [6]. In addition, ZIBs are inherently safer since aqueous electrolytes are used rather than the flammable organic electrolytes. The use of an aqueous electrolyte also supports a 100-fold increase in ionic conductivity, resulting in high power capability. Under mildly acidic aqueous electrolytes, Zn metal does not form an intermediate phase such as hydroxides and oxide, but immediately oxidizes to zinc ions, and reversible plating and stripping is possible due to a large overpotential against hydrogen gas generation. Considering the narrow operating potential window of aqueous electrolytes, which are inherently limited by the electrolysis of water, Zn has the advantage of readily being used directly as the metal anode in aqueous environments, and also offers a high theoretical capacity (820 mAh g^{-1}, 5854 mAh L^{-1}) at an appropriate redox potential (-0.76 V vs. SHE) [7].

Despite such merits, there are some limitations that must be considered for developing aqueous ZIBs. Electrodeposition of Zn occurs non-uniformly due to localized nucleation and irregular crystal growth. The shape of electrodeposited Zn varies depending on the reaction conditions, but typically has a fragile dendrite shape. The dendrite particles act as a localized point where electric charge accumulates, which further accelerates the growth of the dendrite [8]. As the overgrown dendrites become dislodged from the Zn metal surface, the particles become electrically de-activated or pierce through the separator to cause a short circuit [9]. The second challenge associated with aqueous ZIBs is the generation of hydrogen gas that results in evaporation of the electrolyte, thus driving forward the hydration of Zn cations that ultimately forms zinc hydroxide ($Zn(OH)_2$). This side reaction leads to a high overpotential for Zn plating and stripping that reduces the Coulombic efficiency [10]. The spontaneous corrosion reaction of Zn metal is also considered to be a major factor that hinders the performance of ZIBs in the context of self-discharge [11]. As a result of this reaction, a passivating film is formed on the surface that inhibits electrochemical reaction by increasing the hydroxide ion concentration in solution [12]. Based on the aforementioned challenges, it is essential to solve corrosion issues of Zn metal and minimize reduction in surface reactivity to increase the efficiency of the ZIBs.

Several strategies have been proposed to address these critical issues. There are studies on the use of weak acid electrolytes, such as zinc sulfate ($ZnSO_4$) [13], zinc chloride ($ZnCl_2$) [14], zinc nitrate ($Zn(NO_3)_2$) [4], zinc trifluoromethanesulfonate ($Zn(CF_3SO_3)_2$) [15], sputtering of gold nanoparticles [16] and carbon-zinc composites [17], and modification of electrode surfaces with materials such as carbon nanotubes [18], graphene oxides [19], polyamides [20], calcium carbonate ($CaCO_3$) [21], titanium oxide (TiO_2) [22], aluminum oxide (Al_2O_3) [23], and 3D zinc oxide (ZnO) [24]. In addition, Wang et al. conducted a study using a separate host rather than bare Zn, which provided higher capacity and Coulombic efficiency [25]. Atomic layer deposition (ALD) is a versatile deposition technique capable of forming conformal and uniform thin films with atomic level precision [23], the key benefit of which is negligible addition on the weight of the electrode upon surface treatment of a few nanometer thick ALD based thin films. Mai et al. first applied ALD TiO_2 coating as a protective layer on Zn anodes where an amorphous TiO_2 layer enhanced the electrochemical performance of ZIB [22]. Thereafter, Liu et al. coated Al_2O_3, a commercially relevant ALD processed material, and investigated the effect of this protective film coating at varying thicknesses [23]. SnO_2 has been occasionally used as protective layer in other fields of research [26, 27] but has never been explored as a protective layer for ZIBS anode to date.

In this study, SnO_2 was uniformly coated onto Zn metal anodes (SnO_2@Zn) using ALD to avoid direct contact between the aqueous electrolyte and electrode surface. This interlayer suppresses the generation of hydrogen gas and also mitigates the propensity for zinc dendrite growth [28]. Scheme 1 illustrates the differences in Zn plating and stripping between bare Zn foil and SnO_2@Zn foil where the latter shows more homogenous zinc deposition. Herein, to validate the impact of the protective SnO_2 layer we perform an exhaustive electrochemical analysis of the differences between bare Zn and SnO_2@Zn in terms of zinc plating/stripping, cycle life, and performance in full-cell configurations paired with manganese oxide.

We also perform density functional theory (DFT) calculations to compute the adsorption energy of the Zn atoms on the surfaces of Zn foil with and without the SnO_2 layer. Through these calculations, we confirm that the adsorption energy on bare Zn is lower than that of SnO_2@Zn; thus, supporting our hypothesis that the use of SnO_2 as an interlayer at the anode/electrolyte interface inhibits dendrite growth.

Experimental And Methods

Preparation of SnO_2@Zn via Atomic Layer Deposition

A 0.1 mm thick zin foil (99.9994%, Thermo Fisher) was used directly as a bare Zn electrode. A 10-nm thick SnO_2 thin film was deposited onto the Zn foil (milled to a thickness of 50 μm) using a commercial ALD reactor (Savannah S200, Veeco Instruments Inc., Massachusetts, USA). The chamber was kept at 125°C, which was purged under flowing N_2 (90 sccm) prior to each deposition. Tetrakis(dimethylamino)tin (TDMASn) and deionized water (H_2O) were used as precursors with a full ALD cycle consisting of a t1 - t2 - t3 - t4 sequence, where t1 corresponds to the H_2O pulse length, t2 the N_2 purge time, t3 the TDMASn pulse length, and t4 the N_2 purge time. In all cases, t1, t2, t3, and t4 were kept constant at 0.015 s, 10 s, 1.0 s, 10 s, respectively. Growth rate was monitored by in-situ quartz crystal microbalance (QCM), which was further verified by measuring the final thickness of SnO_2 thin film deposited on a witness Si wafer via spectroscopic ellipsometry (Nano-View, Korea). Based on the growth rate (0.63 Å cycle^{-1}), the process was repeated for 160 cycles to achieve 10 nm films.

Synthesis of α-MnO_2

Manganese oxide (α-MnO_2) was synthesized using a hydrothermal synthesis method. 0.09878 g of $KMnO_4$ (Junsei) and 0.4226 g of $MnSO_4 \cdot H_2O$ (Sigma Aldrich) were dissolved in 80 mL of deionized water and the dark solution was placed in 100 mL Teflon autoclave with subsequent heating at 160 °C for 12 h. After the mixture was cooled to room temperature, it was washed by centrifugation using generous amount of deionized water and ethanol prior to an overnight drying process at 180 °C in a (conventional or vacuum) oven.

Computational calculations

First principles calculations were preformed using density functional theory (DFT) as implemented in the Vienna Ab initio Simulation Package (VASP) [29]. The projector augmented wave method (PAW) was used for the core and valence electron interactions [30], and Perdew-Burke-Ernzerhof (PBE) generalized gradient approximation (GGA) was used for the exchange-correlation energy functional. Plane wave basis set was used for the calculations with an energy cutoff of 500 eV. The convergence criteria for the electronic self-consistency loop and the ionic relaxation loop were $10-5$ eV and 0.03 eV Å^{-1}, respectively. The lowest surface energy slabs, Zn (0001) and SnO_2 (110), were used for the calculations with 64 and 108 atoms, respectively. A vacuum layer of 25 Å was included to prevent the interaction between slabs, and a gamma-centered 6×6×1 k-point mesh was used for the calculations. The atoms in the bottom

layers below half of the slab were fixed for their bulk-like positions. The adsorption energy of Zn, E_ads, was determined as E_ads=E_all-E_substrate-E_Zn, where E_all, E_substrate, and E_Zn are total energies of all system, substrate, and Zn atom, respectively. The difference of charge density was obtained as Δρ=ρ_all-ρ_substrate-ρ_Zn, where ρ_all, ρ_substrate, and ρ_Zn are charge density of all system, substrate, and Zn atom, respectively. Positive and negative values of Δρ indicate the charge accumulation and depletion, respectively.

Materials Characterization

To verify the crystal structure of zinc electrodes with and without SnO_2 coating, X-ray powder diffraction (XRD) was measured on a Bruker D8 ADVANCE X-ray diffractometer using a Cu Kα (1.5418 Å) source operated at 40 kV and 40 mA, and at an incidence angle of 1°. X-ray Photoelectron Spectroscopy (XPS) analysis was performed using a micro-focus monochromatic Al Kα radiation (1,486.6 eV) of Nexa (Thermo Fisher Scientific). It was used to investigate the properties of SnO_2 thin films deposited via ALD. To quantify wettability of electrolyte on the zinc electrodes, contact angle measurements were performed using contact angle goniometer (Ossila). Field emission scanning electron microscopy (FE-SEM) was used to identify the morphology of Zn dendrite growth. The microstructures were examined using FE-SEM (Inspect F, FEI Company) equipped with an Energy Dispersive X-ray spectroscopy (EDS, Ultim Max). The anti-corrosion effect was analyzed using Tafel polarization measurements in a three-electrode system. Zn metal, graphite and saturated calomel electrodes (SCE) were used as working, counter, and reference electrodes, respectively, in an aqueous 2 M $ZnSO_4$ electrolyte. The corrosion potentials and currents were measured at a scan rate of 3.0 mV s^{-1} (Bio-Logic Science Instruments, VMP3 type).

Electrochemical Characterization

The α-MnO_2 electrode used as a cathode was prepared by mixing active material (α-MnO_2), super P (MTI Korea), and polyvinyldifluoride (PVDF, Sigma Aldrich) in a ratio of 7:2:1. The slurry was ball milled and casted onto a titanium foil current collector using a 375 μm doctor blade. Finally, the sample was dried in an oven at 60 °C for at least 12 h and stored in a vacuum oven. The mass loading was maintained at 2–2.5 mg cm^{-2}. Zn||Zn symmetric cells and Zn||MnO_2 cells were fabricated in a 2032 type coin cell to identify electrochemical properties. Zn||Zn symmetric cells were assembled using the same zinc electrode on both sides and 2 M $ZnSO_4$ was used as an electrolyte. The Zn||MnO_2 cell for electrochemical evaluation used CR2032 coin-cells with a 3 M $Zn(CF_3SO_3)_2$ electrolyte. In the Zn||MnO_2 cell, an additional carbon filter was added to compensate for the dissolution of Mn^{2+} in the MnO_2 electrode. All Zn||Zn symmetric cells and Zn||MnO_2 cells were operated using a galvanostat (WonATech) at various current densities. Every cell had a resting time of 8 h before operation for stabilization of the cells. Zn||MnO_2 cells were tested between operating voltages of 0.8 and 1.8 V (vs. Zn/Zn^{2+}). Electrochemical impedance spectroscopy (EIS) was carried out using a multichannel potentiostat analyzer (Bio-Logic Science Instruments, VMP3 type). EIS measurements were conducted at an amplitude perturbation signal of 0.1 mV. The nonlinear least-squares method provided in Z-view

software (Scribner Associates, Inc.) was used for the fitting process of the Nyquist plot. Cyclic voltammetry (CV) measurements were carried out at a scan rate of 0.1 mV s^{-1}. Differential electrochemical mass analysis (DEMS) analysis was used to compare hydrogen gas generation. Zn-Zn symmetric cells were fabricated with 2032 coin cells with a diameter of 0.5 mm and identified by HS cell. A SUS mesh was used for even gas delivery, and the H$_2$ gas produced by the side reaction of zinc was measured using the argon carrier gas of HS Cell. H$_2$ gas generated after releasing the remaining air in the HS Cell for 30 min and maintaining the HS cell in a closed state for 10 h was identified. A preliminary experiment was conducted to see if the degree of hydrogen generation inside the cell could be confirmed by DEMS analysis. The DEMS analysis was all composed of symmetric cells. This was done using a coin cell with a hole to allow gas to pass through, and analyzed for a total of 30 h (three cycles of 10 h). The valve was opened for 2 min to analyze the gas generated within 10 h.

Results And Discussion

Materials Characterization of SnO$_2$@Zn

Tin oxide coated zinc (SnO$_2$@Zn) sample was prepared using atomic layer deposition (ALD) at 125 °C with a growth rate of 0.63 Å per cycle to achieve a 10-nm thick SnO$_2$ film. To verify the presence of the SnO$_2$ layer on the surface of the Zn foil, we first performed X-ray diffraction on two respective samples, bare Zn foil and SnO$_2$@Zn (Fig. 1a). For both Bare Zn and SnO$_2$@Zn samples, the main diffraction peaks observed at 36°, 38°, 43°, and 54° are indexed to the (002), (100), (101), and (102) reflections associated with hexagonally close packed structure of zinc. This confirms that our SnO$_2$ coating method does not affect the structure of the bulk, and Zn is present as the predominant phase. We did not observed peaks related to SnO$_2$ because the thickness of SnO$_2$ layer is below the detection limit. Therefore, X-ray photoelectron spectroscopy (XPS) was performed to investigate the chemical state (or local binding environment) of the SnO$_2$@Zn sample at binding energies ranging from 480 to 505 eV to monitor the Sn 3d region. After performing ALD, we observe a stark difference between the spectra for bare Zn and SnO$_2$@Zn samples, where the latter exhibits an additional peak at 487.38 eV in the Sn 3d$_{5/2}$ region, which is absent in the bare Zn foil (Fig. 1b and 1c) [31]. This symmetric peak is associated with the presence of SnO$_2$ on the surface. In addition, high resolution fitting of the Sn 3d XPS spectrum shows that the SnO$_2$ layer is composed of 91 % SnO$_2$ and 9 % metallic Sn (Fig. 1d). Both XRD and XPS results indicate that the formation of ALD based SnO$_2$ layer on the surface of Zn foil occurs without perturbing the bulk of the Zn foil.

The wettability between the electrolyte and the zinc metal surface is yet another important consideration as improved surface wettability leads to a more uniform Zn^{2+} flux on the surface [32]. This assists in improving the electrochemical performance by lowering the charge-transfer resistance during plating/stripping. The wettability of the bare Zn and SnO$_2$@Zn surfaces were measured by examining the contact angle after dropping 10 µL of 2 M ZnSO$_4$ electrolyte. In the presence of the SnO$_2$ coating, the

surface wettability is improved as verified by the decrease in contact angle from 95.85° for bare Zn to 75.68° for SnO$_2$@Zn (Fig. 1e and 1f). The result indicates that the surface of SnO$_2$@Zn is more favorable for Zn^{2+} plating/stripping. Before we proceeded to electrochemical cycling, corrosion curves were measured to analyze corrosion behavior (or kinetics) in the mild acidic electrolyte (2 M ZnSO$_4$) for both bare Zn and SnO$_2$@Zn as shown in Fig. S1. The calculated corrosion kinetic parameters and corrosion inhibition efficiencies are tabulated in Table S1. The calculated corrosion inhibition efficiency P_p of the coated electrodes relative to the uncoated version was 28.47%. This analysis also shows that the SnO$_2$ coating reduces the corrosion current (I_{corr}) as the value decrease from 1.62 to 1.16 mA for bare Zn and SnO$_2$@Zn, respectively. This suggests that metal corrosion is alleviated by physically preventing direct contact of the electrolyte with the zinc metal surface. This corrosion mitigation is suspected to be highly beneficial for minimizing hydrogen production [33], which is considered to be a deleterious reaction that results in cell failure causing an increase in the cell pressure.

Electrochemical Characterization

To investigate the effect of the SnO$_2$ coating on the electrochemical properties, symmetric cells of Zn||Zn and SnO$_2$@Zn||SnO$_2$@Zn were fabricated using an electrolyte comprising 2 M ZnSO$_4$. Plate/strip cycles of these symmetric cells were carried out at a current density of 0.25 mA cm^{-2} within a limited capacity of 0.05 mAh cm^{-2} (Fig. 2). A key distinction can be made from the difference in overpotentials between these two materials. The SnO$_2$@Zn symmetric cell yielded stable plating/stripping behavior, as evidenced by a low overpotential of <10 mV for 300 h corresponding to 750 cycles; however, bare Zn exhibits a much higher overpotential of >60 mV even at the initial stages with unstable cycling during the course of 300 h. To further compare the effect of the SnO$_2$ coating, additional plate/strip cycles were conducted at higher current densities ranging from 1 to 5 mA cm^{-2} (Fig. S2). Across all imposed current densities, the overpotentials for SnO$_2$@Zn remain lower than those of the bare Zn, demonstrating that this improvement arises from the protective SnO$_2$ layer.

To further elucidate the mechanisms that are involved in these complex solid/electrolyte interfacial reactions, electrochemical impedance spectroscopy was then performed for bare Zn and SnO$_2$@Zn symmetric cells before cycling and at specific points during their cycle lifetime (5th, 20th and 50th cycle). The impedance spectra were fitted to the equivalent circuit illustrated in Fig. 3a and 3b. The obtained equivalent circuit shows that the fitted EIS spectra matches the raw data well. The Nyquist plots for both electrodes consisted of one or more semicircles. The value of R_{SEI} is related to surface layer resistance of deposited materials (Zn, ZnO, ZnOH$_2$, ZnS etc.) whereas R_{ct} is related to the resistance of the deposited material. It was reported that the morphology of the deposited material had the greatest effect on R_{ct} [34]. For both SnO$_2$@Zn and bare Zn, the values of R_{SEI} are comparable across all cycles; yet, a large difference in the values of R_{ct} are observed between the two samples. The SnO$_2$@Zn sample showed much smaller R_{ct} values than those of bare Zn upon cycling, suggesting that the morphology of the

deposited material on SnO$_2$@Zn becomes more favorable for charge transfer. Furthermore, this trend reveals that the SnO$_2$ coating reduces parasitic reactions between the Zn electrode and the electrolyte during cycling, thereby reducing the overpotential.

Subsequent to electrochemical interrogation of the charge transfer interface for bare Zn and SnO$_2$@Zn, we sought to visualize the electrode surface after cycling (5th, 20th and 50th cycle) via scanning electron microscopy (Fig. 4a and 4b). The re-deposition of zinc platelets was observed in both electrodes, and for SnO$_2$@Zn, in-plane growth of platelets was observed as the cycle progressed. For bare Zn, the growth directions of zinc platelets are randomly oriented and contrary to this growth mechanism, it was confirmed that the deposition of zinc plateltes on the SnO$_2$@Zn surface mainly exhibits in-plane growth. These findings are consistent with the trend observed for R_{ct} from the aforementioned impedance data. As the cycle progresses, the difference in overpotential occurs due to the difference in the growth behavior of Zn on bare Zn and SnO$_2$@Zn.

To understand the directionality component of plating/stripping for SnO$_2$@Zn, grazing incidence X-ray diffraction (GIXRD) was carried out to compare the orientation of the crystal structure of the deposited Zn structure on the surface of bare zinc and SnO$_2$@Zn electrodes (Fig. 5a and 5b). The peak that appears at 36.3° corresponds to the (002) plane of Zn, and the peak that appears at 38.9° is the (100) plane. The ratio of the XRD peak intensity of (002) to the (100) reflection on the electrode surface after cycling yields information on the texturing and orientation of the Zn particulate. The smaller the ratio, the higher the tendency for dendrite growth in an isotropic manner. The ratios for bare Zn and SnO$_2$@Zn are 1.07 and 2.19, respectively, and this quantitative analysis proves that zinc shows a preferential growth as a result of the SnO$_2$ treatment which serves as a feature that mitigates severe dendrite growth.

As discussed earlier regarding corrosion issues that emerge in these electrodes, the propensity for hydrogen gas (H$_2$) generation is yet another key property that should be assessed. To compare H$_2$ gas evolution, differential electrochemical mass spectrometry (DEMS) analysis was performed [35]. The H$_2$ gas generated by the zinc side reaction was measured using an argon carrier gas in an HS Cell. The H$_2$ gas generated was measured after releasing the remaining air in the HS Cell for ~30 min, then maintaining the HS cell in a closed state for 10 h. Symmetric cells were used for both Bare Zn and SnO$_2$@Zn to perform DEMS analysis. This was done using a coin cell with a hole to allow gas to permeate, and analyzed for a total of 30 h (three 10 h cycles). The valve was opened for 2 min and the generated gas was analyzed for10 h. It was confirmed that the released gas was H$_2$ gas, and as shown in Fig. 6, the relative amount of H$_2$ between the two samples can be compared with their relative pressure. It was confirmed that the H$_2$ gas relative pressure generated after the first 10 h was reduced by 41.14% from about   to   in the presence of the SnO$_2$ coating. At longer duration, the difference widens to 58.26% and 90.30%. This is in agreement with the previously confirmed cycling and impedance data, and it can be seen that the SnO$_2$ coating leads to directional zinc growth, thereby reducing side reactions and suppressing the generation of H$_2$ gas.

First principles calculations were performed to determine the adsorption energy of a Zn atom on Zn and SnO_2. Fig. 7a and 7b show the optimized geometries of Zn adsorption on the Zn (0001) and SnO_2 (110) surfaces. The adsorption energies of Zn on the Zn (0001) and SnO_2 (110) are -0.25 and -1.42 eV, respectively, indicating that the SnO_2 surface exhibits stronger adsorption of a Zn atom. This result is consistent with the experimental results that Zn ions prefer to bind on the surface of SnO_2. Atomic configurations of Zn adsorption on Zn (0001) and SnO_2 (110) slab are also shown in Fig. S3 with the view along z direction. The charge density difference plot in Fig. 7c indicates the strong interaction between Zn atom and O atom on the SnO_2 (110) by the charge transfer from the Zn to O atoms.

To validate the effect of SnO_2 coating on Zn adsorption, the surface morphology of bare Zn and SnO_2@Zn after depositing a certain amount of zinc (1 mA cm^{-2} for 2 h) was observed by ex situ SEM (Fig. 8a and 8b). On the surface of bare zinc after deposition, there are many spherical lumps in which zinc particulates are aggregated. There are two distinct types of zinc lumps, densely packed zinc and a composite of plate and wire shaped zinc as shown in Fig. S4. The EDS mapping results (Fig. S5 and S6) confirm that two types of lump are mainly composed of zinc. It is noteworthy that some plate-like zinc particles show high amounts of oxygen and sulfur in the EDS maps (Fig. S7). The result indicates that some plate-shaped zinc particles can be insulating zinc sulfate hydroxide [36]. Compared to the surface of bare Zn, there are less lumps and plate-shaped zinc on the surface of SnO_2@Zn. Furthermore, the deposited zinc particulates on SnO_2@Zn show a much smaller size and uniform size distribution than those of bare Zn. The cross-section image of bare Zn shows spherical zinc aggregates on bare Zn having a diameter of ~ 40 μm. Contrary to this observation, SnO_2@Zn has no such aggregates. These results strongly suggest that the smaller adsorption energies of Zn on the SnO_2 than bare Zn, which we have calculated by DFT, may be helpful in providing homogeneous nucleation sites, resulting in a uniform and isotropic manner for Zn growth on the surface. The isotropic growth of Zn on the surface is not only effective in inhibiting dendrite growth, but also effective in improving Zn ion diffusion on the surface. We speculate that these features will improve the cycle and rate performance of a full cell.

Full Cell Performance

To integrate the advances in anode performance into a full cell, a full cell comprising SnO_2@Zn and bare Zn was paired with manganese oxide (α-MnO_2) as the cathode. Cyclic voltammetry (CV) was first used as an initial assessment of the redox activity and reversibility of bare Zn||MnO_2 and SnO_2@Zn||MnO_2 cells over 10 cycles at 0.1 mV s^{-1} (Fig. S9a and S9b). There are two pairs of redox peaks in the voltammetric signatures for bare Zn||MnO_2 and SnO_2@Zn||MnO_2. It is evident that the redox peaks of each sample show similar reaction behavior, which does not affect the mechanism of the MnO_2 redox reaction due to ALD treatment. Though a smaller peak voltage separation can be observed for SnO_2@Zn||MnO_2, further testing in the form of constant current charge/discharge measurements are needed to understand rate capability.

Fig. 9a, 9b, and 9c show the rate capability of $Zn||MnO_2$ and $SnO_2@Zn||MnO_2$ from 0.1 A g^{-1} to 1 A g^{-1}. Consistent with the voltammetric results, the voltage profile results also prove that each sample yields a similar redox reaction (Fig. 9a and 9b). For bare $Zn||MnO_2$, 0.1 A g^{-1} supported a discharge capacity of 176.9 mAh g^{-1}. At increasing current densities, discharge capacities of 154.9, 139.9, 124 and 98.7 mAh g^{-1} were delivered in the order of 0.2, 0.3, 0.5, and 1 A g^{-1}. For $SnO_2@Zn||MnO_2$, discharge capacities of 211, 183, 166.2, 151.3, 126.3 mAh g^{-1} were achieved in order from 0.1−1 A g^{-1}. $SnO_2@Zn||MnO_2$ offered improved rate performance (Fig. 9c). Fig. 9d shows the cycling performance of $Zn||MnO_2$ and $SnO_2@Zn||MnO_2$ at 1 A g^{-1}. The bare $Zn||MnO_2$ cell was short circuited at 1100 cycles, whereas $SnO_2@Zn||MnO_2$ cell maintains the capacity after 1100 cycles. Therefore, $SnO_2@Zn||MnO_2$ cells have far superior cycling stability than bare $Zn||MnO_2$. These results clearly illustrate that the rate performance and cycle stability of $Zn||MnO_2$ systems have improved due to SnO_2 coating.

Conclusion

In the present study, we demonstrate that the application of a SnO_2 protective layer on a zinc metal electrode for an aqueous ZIB is effective in reducing overpotential and suppressing the hydrogen gas generation resulting from surface parasitic reactions. In addition, we theoretically prove that SnO_2 is effective in driving forth uniform zinc growth by density functional theory calculations. Through an exhaustive experimental interrogation, our theoretical calculations suggesting efficient zinc plating/stripping was validated. We then turned our attention to the effect of suppressing the hydrogen gas generation in addition to the effect of driving forth uniform zinc growth with a nanoscale protective layer on the Zn surface. The rigorous analyses performed in this study demonstrate the critical parameter space that must be considered for the development of aqueous ZIBs, which are H_2 gas suppression, protective layer coatings, mitigating dendrite growth by isotropic manner growth of zinc, and full cell evaluation.

Declarations

References

1. Liu Y, Lu X, Lai F et al (2021) Rechargeable aqueous Zn-based energy storage devices. Joule 5(11):2845-2903 https://doi.org/10.1016/j.joule.2021.10.011

2. Levi E, Gofer Y and Aurbach D (2010) On the way to rechargeable Mg batteries: the challenge of new cathode materials. Chem. Mater. 22(3):860-868 https://doi.org/10.1021/cm9016497

3. Kim S, Yin L, Lee M et al (2020) High-voltage phosphate cathodes for rechargeable Ca-ion batteries. ACS Energy Lett. 5(10):3203-3211 https://doi.org/10.1021/acsenergylett.0c01663

4. Xu C, Li B, Du H et al (2012) Energetic zinc ion chemistry: the rechargeable zinc ion battery. Angew. Chem. 124(4):957-959 https://doi.org/10.1002/ange.201106307

5. Lin M-C, Gong M, Lu B et al (2015) An ultrafast rechargeable aluminium-ion battery. Nature 520(7547):324-328 https://doi.org/10.1038/nature14340

6. Konarov A, Voronina N, Jo J H et al (2018) Present and future perspective on electrode materials for rechargeable zinc-ion batteries. ACS Energy Lett. 3(10):2620-2640 https://doi.org/10.1021/acsenergylett.8b01552

7. Shin J, Lee J, Park Y et al (2020) Aqueous zinc ion batteries: focus on zinc metal anodes. Chem. Sci. 11(8):2028-2044 https://doi.org/10.1039/D0SC00022A

8. Zhang N, Huang S, Yuan Z et al (2021) Direct self-assembly of MXene on Zn anodes for dendrite-free aqueous zinc-ion batteries. Angew. Chem. 133(6):2897-2901 https://doi.org/10.1002/ange.202012322

9. Yufit V, Tariq F, Eastwood D S et al (2019) Operando visualization and multi-scale tomography studies of dendrite formation and dissolution in zinc batteries. Joule 3(2):485-502 https://doi.org/10.1016/j.joule.2018.11.002

10. Borchers N, Clark S, Horstmann B et al (2021) Innovative zinc-based batteries. J. Power Sources 484:229309 https://doi.org/10.1016/j.jpowsour.2020.229309

11. Baugh L.M. (1979) Corrosion and polarization characteristics of zinc in neutral—acid media—I. pure zinc in solutions of various sodium salts. Electrochim. Acta 24(6):657-667 https://doi.org/10.1016/0013-4686(79)87048-6

12. Tribbia M, Glenneberg J, Zampardi G et al Highly efficient, dendrite-free zinc electrodeposition in mild aqueous zinc-ion batteries through indium-based substrates. Batteries & Supercaps 5(5) https://doi.org/10.1002/batt.202100381

13. Zhou J, Shan L, Wu Z et al (2018) Investigation of V_2O_5 as a low-cost rechargeable aqueous zinc ion battery cathode. ChemComm 54(35):4457-4460 https://doi.org/10.1039/C8CC02250J

14. Zhang C, Holoubek J, Wu X et al (2018) A $ZnCl_2$ water-in-salt electrolyte for a reversible Zn metal anode. ChemComm 54(100):14097-14099 https://doi.org/10.1039/C8CC07730D

15. Zhang N, Cheng F, Liu Y et al (2016) Cation-deficient spinel $ZnMn_2O_4$ cathode in Zn (CF_3SO_3) 2 electrolyte for rechargeable aqueous Zn-ion battery. J. Am. Chem. Soc. 138(39):12894-12901 https://doi.org/10.1021/jacs.6b05958

16. Cui M, Xiao Y, Kang L et al (2019) Quasi-isolated Au particles as heterogeneous seeds to guide uniform Zn deposition for aqueous zinc-ion batteries. ACS Appl. Energy Mater. 2(9):6490-6496 https://doi.org/10.1021/acsaem.9b01063

17. Li H, Xu C, Han C et al (2015) Enhancement on cycle performance of Zn anodes by activated carbon modification for neutral rechargeable zinc ion batteries. J. Electrochem. Soc. 162(8):A1439 https://doi.org/10.1149/2.0141508jes

18. Gao X, Yin W and Liu X (2021) Carbon nanotubes-based electrode for Zn ion batteries. Mater. Res. Bull. 138:111246 https://doi.org/10.1016/j.materresbull.2021.111246

19. Zhou Z, Zhang Y, Chen P et al (2019) Graphene oxide-modified zinc anode for rechargeable aqueous batteries. Chem. Eng. Sci. 194:142-147 https://doi.org/10.1016/j.ces.2018.06.048

20. Zhao Z, Zhao J, Hu Z et al (2019) Long-life and deeply rechargeable aqueous Zn anodes enabled by a multifunctional brightener-inspired interphase. Energy Environ. Sci. 12(6):1938-1949 https://doi.org/10.1039/C9EE00596J

21. Kang L, Cui M, Jiang F et al (2018) Nanoporous $CaCO_3$ coatings enabled uniform Zn stripping/plating for long-life zinc rechargeable aqueous batteries. Adv. Energy Mater. 8(25):1801090 https://doi.org/10.1002/aenm.201801090

22. Zhao K, Wang C, Yu Y et al (2018) Ultrathin surface coating enables stabilized zinc metal anode. Adv. Mater. Interfaces 5(16):1800848 https://doi.org/10.1002/admi.201800848

23. He H, Tong H, Song X et al (2020) Highly stable Zn metal anodes enabled by atomic layer deposited Al_2O_3 coating for aqueous zinc-ion batteries. J. Mater. Chem. 8(16):7836-7846 https://doi.org/10.1039/D0TA00748J

24. Xie X, Liang S, Gao J et al (2020) Manipulating the ion-transfer kinetics and interface stability for high-performance zinc metal anodes. Energy Environ. Sci. 13(2):503-510 https://doi.org/10.1039/C9EE03545A

25. Wang Z, Huang J, Guo Z et al (2019) A metal-organic framework host for highly reversible dendrite-free zinc metal anodes. Joule 3(5):1289-1300 https://doi.org/10.1016/j.joule.2019.02.012

26. Kim D H, Shin D-Y, Lee Y-G et al (2018) Effects of SnO_2 layer coated on carbon nanofiber for the methanol oxidation reaction. Ceram. Int. 44(16):19554-19559 https://doi.org/10.1016/j.ceramint.2018.07.199

27. Munteanu C, Caldararu M, Bratan V et al (2012) Electrical and catalytic properties of SnO_2/TiO_2 measured in operando conditions. React. Kinet. Mech. Catal. 105(1):13-22 https://doi.org/10.1007/s11144-011-0365-

28. Cao J, Zhang D, Zhang X et al (2022) Strategies of regulating Zn^{2+} solvation structures for dendrite-free and side reaction-suppressed zinc-ion batteries. Energy Environ. Sci. https://doi.org/10.1039/D1EE03377H

29. Kresse G and Furthmüller J (1996) Efficient iterative schemes for ab initio total-energy calculations using a plane-wave basis set. Phys. Rev. B 54(16):11169

https://doi.org/10.1103/PhysRevB.54.11169

30. Blöchl P E (1994) Projector augmented-wave method. Physical review B 50(24):17953 https://doi.org/10.1103/PhysRevB.50.17953

31. Wang W, Huang G, Wang Y et al (2022) Organic acid etching strategy for dendrite suppression in aqueous zinc-ion batteries. Adv. Energy Mater. 12(6) 2102797 https://doi.org/10.1002/aenm.202102797

32. Li B, Xue J, Han C et al (2021) A hafnium oxide-coated dendrite-free zinc anode for rechargeable aqueous zinc-ion batteries. J. Colloid Interface Sci. 599:467-475 https://doi.org/10.1016/j.jcis.2021.04.113

33. Bayaguud A, Fu Y and Zhu C (2022) Interfacial parasitic reactions of zinc anodes in zinc ion batteries: underestimated corrosion and hydrogen evolution reactions and their suppression strategies. J. Energy Chem. 64:246-262 https://doi.org/10.1016/j.jechem.2021.04.016

34. Kao-ian W, Pornprasertsuk R, Thamyongkit P et al (2019) Rechargeable zinc-ion battery based on choline chloride-urea deep eutectic solvent. J. Electrochem. Soc. 166(6):A1063 https://doi.org/10.1149/2.0641906jes

35. Zhou J, Xie M, Wu F et al (2021) Ultrathin surface coating of nitrogen-doped graphene enables stable zinc anodes for aqueous zinc-Ion batteries. Adv. Mater. 33(33):2101649 https://doi.org/10.1002/adma.202101649

36. Sun W, Wang F, Zhang M et al (2021) A rechargeable zinc-air battery based on zinc peroxide chemistry. Science 371(6524):46-51 https://doi.org/10.1126/science.abb9554

Scheme

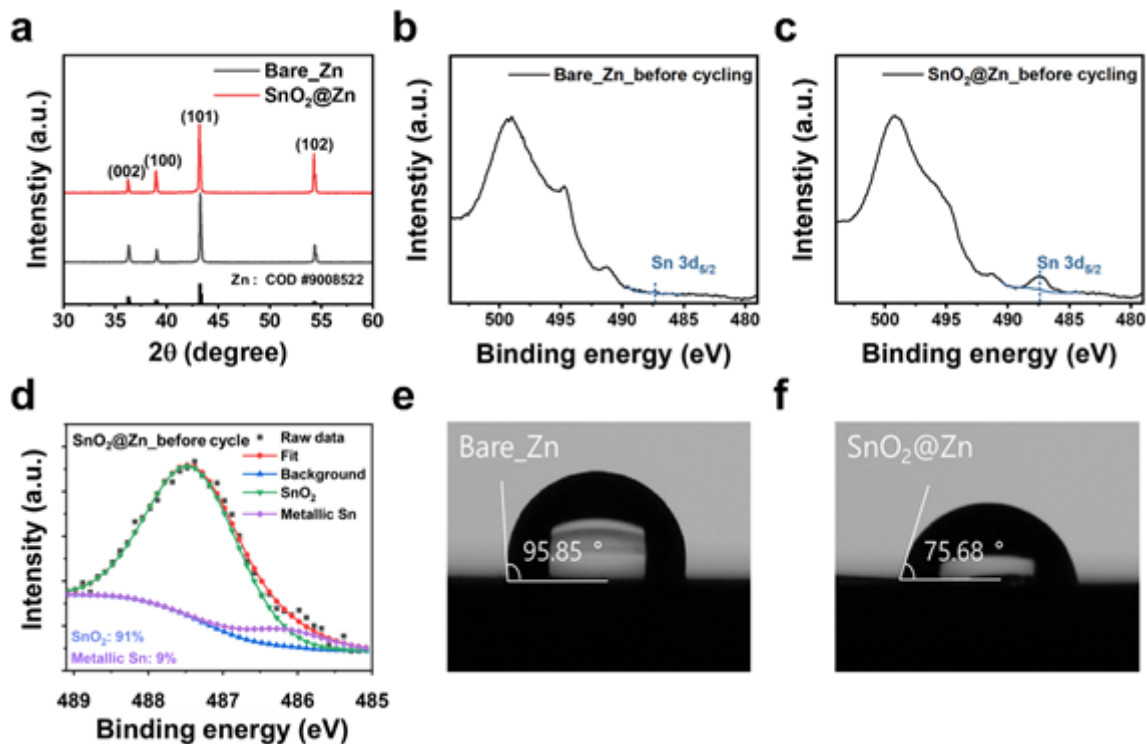Scheme 1 is available in supplementary section.

Figures

Figure 1

a X-ray diffraction patterns of Bare Zn and SnO_2@Zn. X-ray photoelectron spectra collected for the Sn 3d region for **b** Bare Zn, **c** SnO_2@Zn, and **d** Sn 3d $_{5/2}$ region for SnO_2@Zn. Contact angle measurements of **e** Bare Zn, **f** SnO_2@Zn with 2M $ZnSO_4$
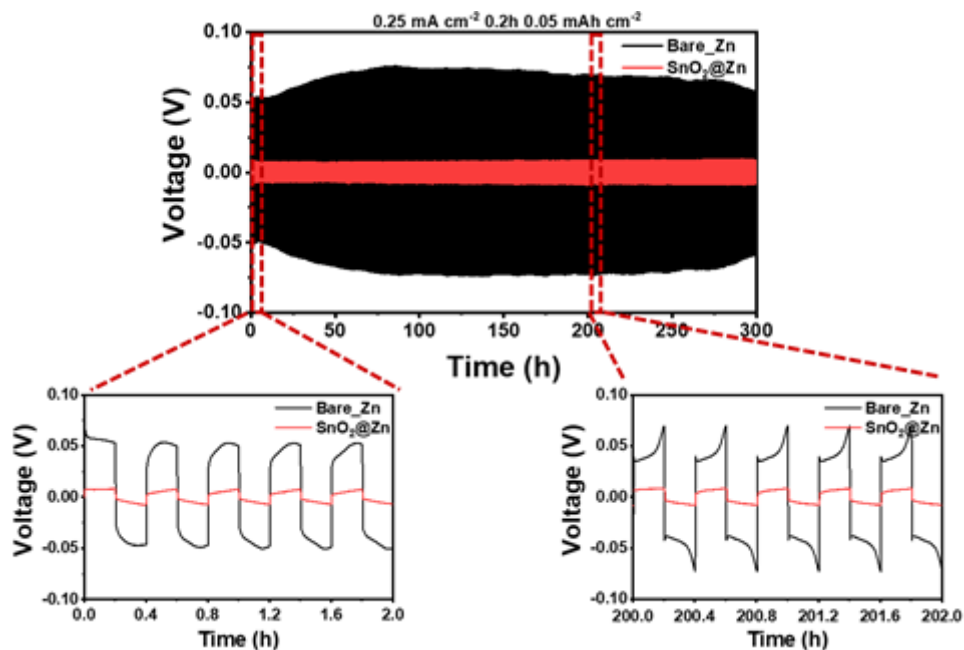

Figure 2

Galvanostatic discharge/charge profiles of Zn symmetric cells using Bare Zn and SnO$_2$@Zn at a current density of 0.25 mA cm^{-2} within a limited capacity of 0.05 mAh cm^{-2}
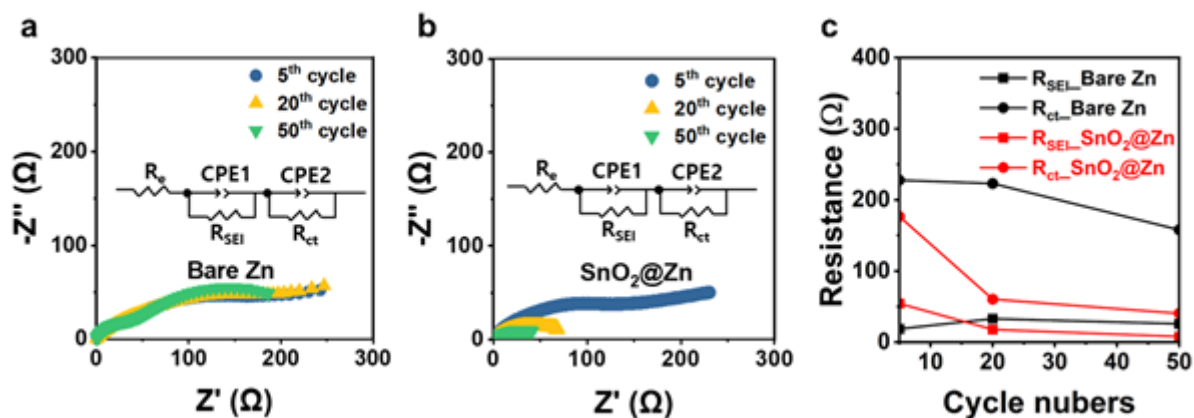

Figure 3

Impedance spectra of symmetric Zn||Zn cells with **a** Bare Zn and **b** SnO$_2$@Zn. Inset: the equivalent circuit model used for fitting **c** Resistance as a function of cycle number based on the impedance fitting results
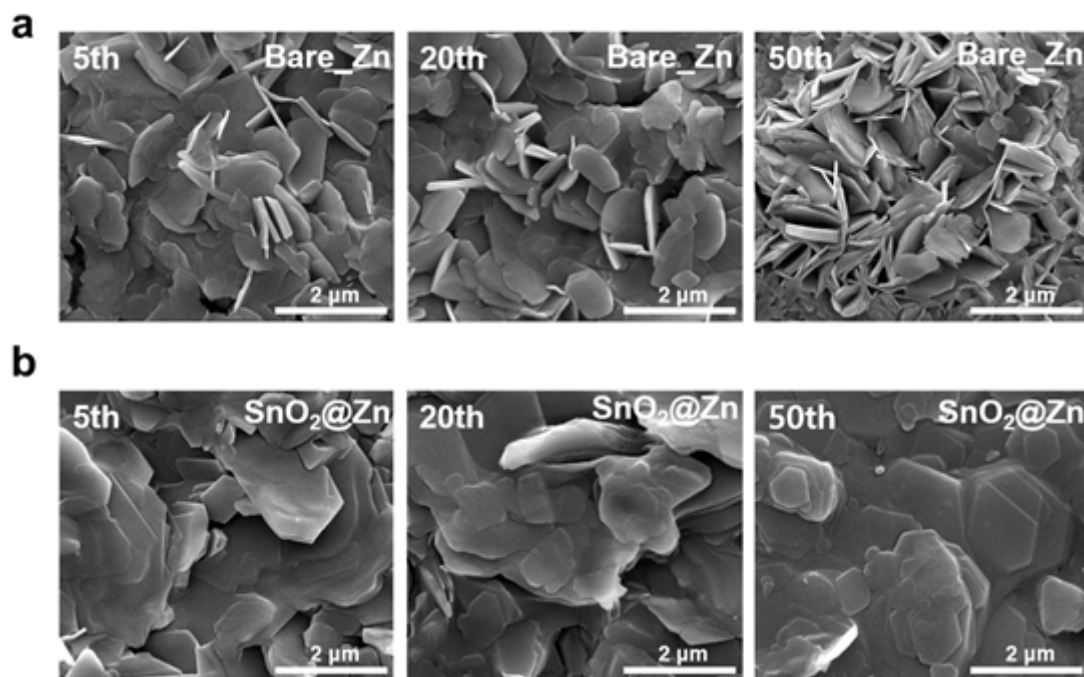
Figure 4

Scanning electron micrographs of Zn deposition after the 5th, 20th, 50th cycle for **a** Bare Zn and **b** SnO$_2$@Zn
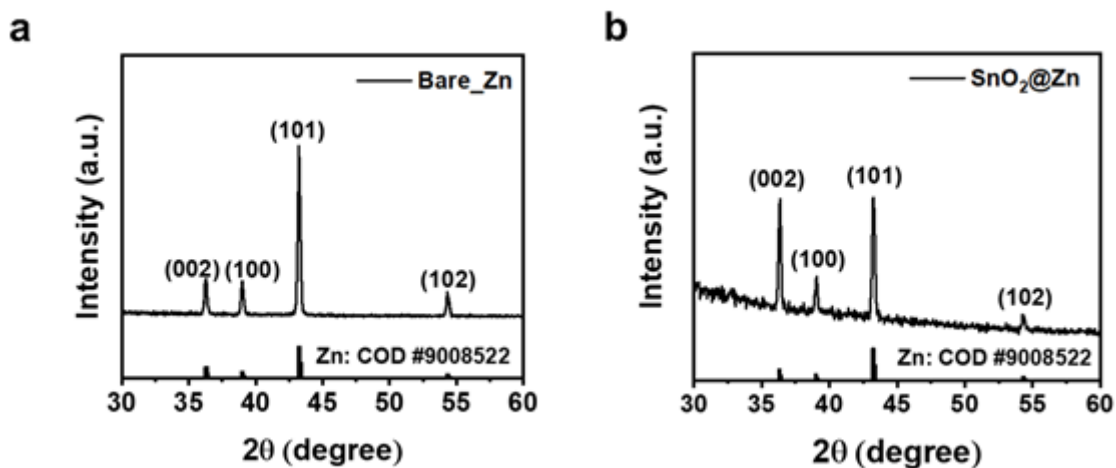
Figure 5

Grazing incidence X-ray diffraction patterns of Zn deposition of **a** Bare Zn and **b** SnO_2@Zn at 1 mA cm^{-2}
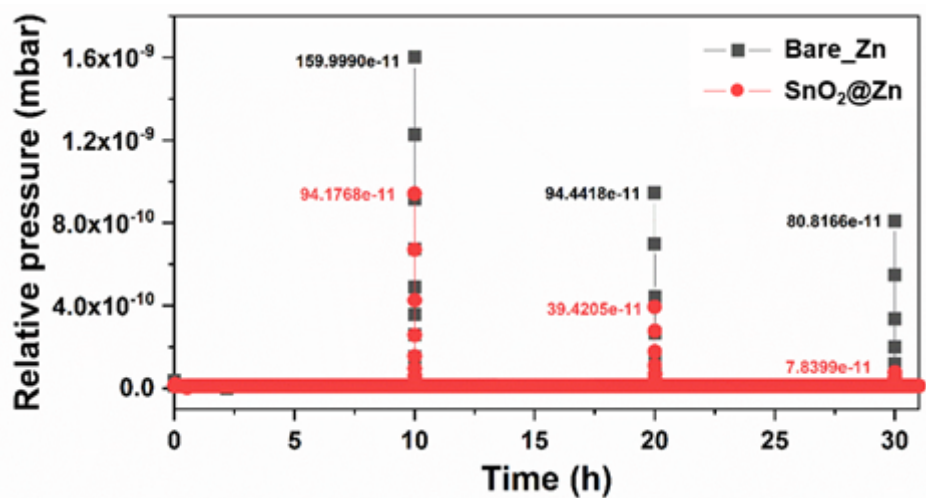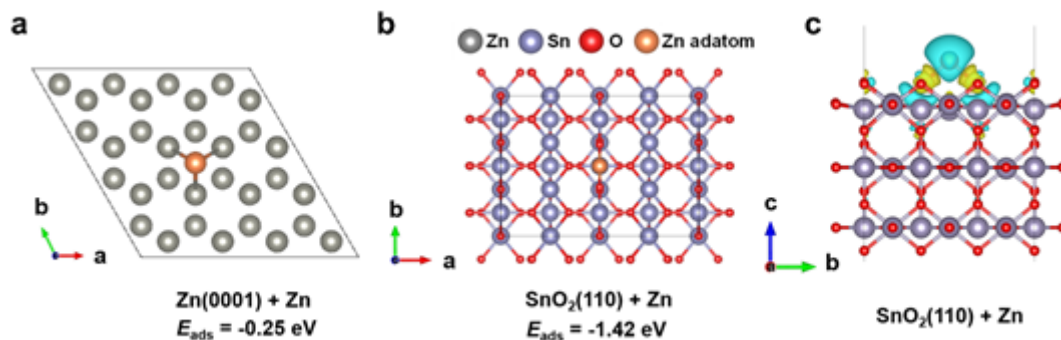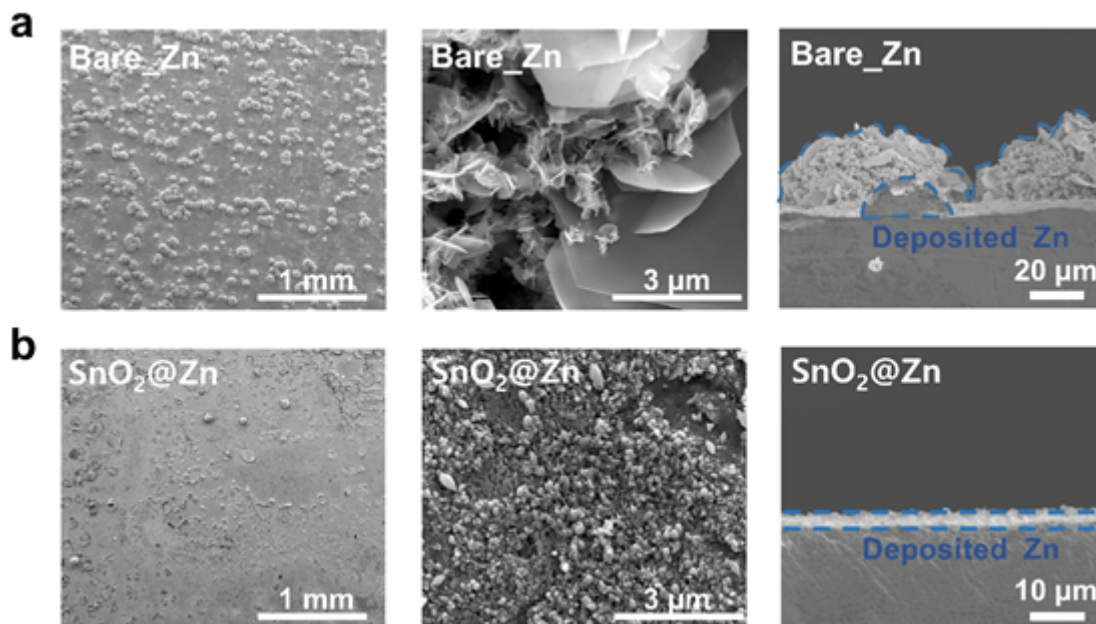

Figure 6

Differential electrochemical mass spectroscopy analysis for measuring H_2 gas generation in a Zn||Zn symmetric cells with Bare Zn and SnO_2@Zn

Figure 7

Atomic configurations of Zn adsorption on **a** Zn (0001) and **b** SnO_2 (110) slab, showing the view normal to the surfaces. Zn, Sn, O atoms and Zn adatom are colored gray, light purple, red, and orange, respectively. **c** Zn adsorption on SnO_2 (110) slab with the charge density difference plot. The yellow and blue regions indicate charge accumulation and depletion, respectively

Figure 8

Scanning electron micrographs for **a** Bare Zn and **b** SnO_2@Zn after depositing a desired amount of Zn (1 mA cm^{-2} for 2 h)
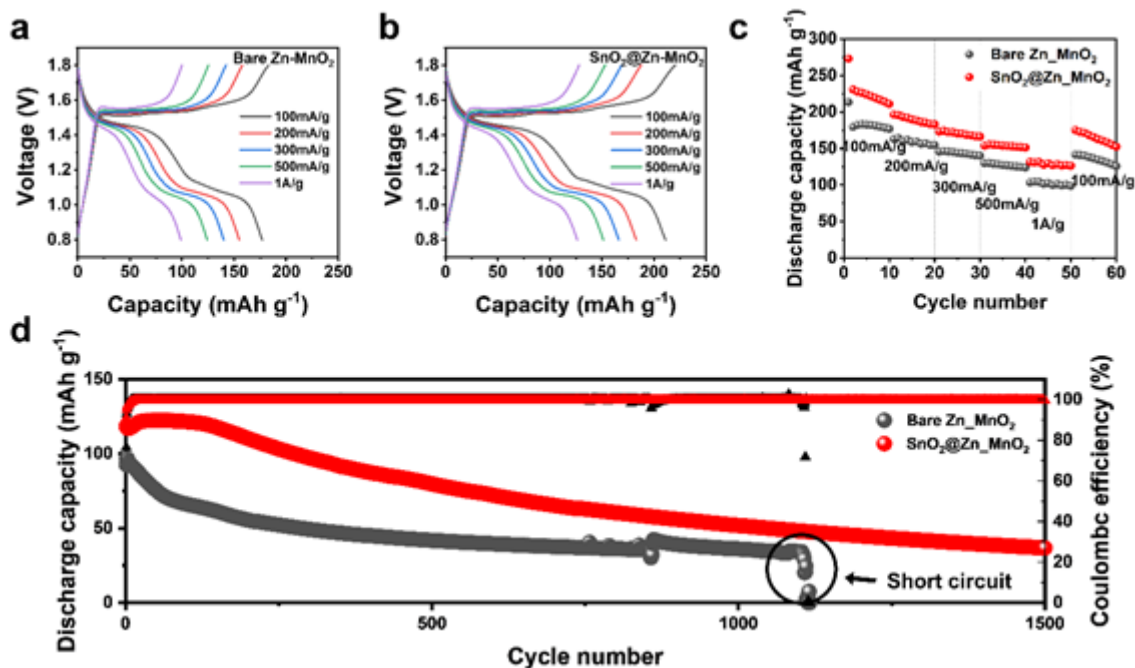
Figure 9

Galvanostatic charge/discharge profiles of **a** Bare Zn||MnO$_2$ cell and **b** SnO$_2$@Zn||MnO$_2$ cell from 100 mA g^{-1} to 1 A g^{-1}. **c** Rate performance of Bare Zn||MnO$_2$ cell and and SnO$_2$@Zn||MnO$_2$ cell from 100 mA g^{-1} to 1 A g^{-1}. **d** Cycling performance of Bare Zn||MnO$_2$ cell and SnO$_2$@Zn||MnO$_2$ cell at a current density of 1 A g^{-1}

Supplementary Files

This is a list of supplementary files associated with this preprint. Click to download.

- SupportingInformation.docx
- Scheme1.png